Solution blow spinning of highly deacetylated chitosan nanofiber scaffolds for dermal wound healing

Nguyen D. Tien[1], Tianxiang Geng[1], Catherine A. Heyward[1], Janne E. Reseland[1], S. Petter Lyngstadaas[1], Jonny J. Blaker[1,2*], Håvard J. Haugen[1*]

[1]Department of Biomaterials, Institute of Clinical Dentistry, University of Oslo, 0317 Oslo, Norway
[2]Department of Materials and Henry Royce Institute, The University of Manchester, Manchester, M13 9PL, United Kingdom

*Correspondence: h.j.haugen@odont.uio.no; jonny.blaker@manchester.ac.uk

Abstract

Biocompatible fibrous scaffolds based on highly deacetylated chitosan were fabricated using high-throughput solution blow spinning. Scanning electron microscopy analyses revealed that the chitosan nanofiber scaffold had ultrafine and continuous submicron fibers (300−1200 nm) with highly interconnected porous structures (30−75% porosity), mimicking some aspects of native extracellular matrix in skin tissue. Post-treatment of as-spun nanofibers with aqueous potassium carbonate solution resulted in a fibrous scaffold having high chitosan content, the fibrous structural integrity could be retained for cell culture. The mechanical properties of chitosan nanofiber scaffolds in dry and wet conditions show their strength and durability to be sufficient for wound-dressing applications. Significantly, the wet scaffold underwent remarkable elastic deformation during stretch, such that the elongation at break dramatically increased up to 44% of its original length, showing wavy fiber morphology near the break site. The culture of normal human dermal fibroblast cells onto scaffolds for 1−14 days demonstrated that the scaffolds were highly compatible and a suitable platform for cell adhesion, viability, and proliferation. Secretion profiles of wound healing-related proteins to the cell culture medium demonstrate chitosan fibers as a promising scaffold for wound healing applications. Overall, the dense fibrous network with high porosity of the chitosan nanofiber scaffold in synergy with appropriate mechanical properties could be suitably applied to design and fabricate new materials that mimic the epidermis layer of natural skin structure.

Keywords: Chitosan nanofibers, solution blow spinning, wound healing, skin tissue engineering, biomaterial

1. **Introduction**

Scaffolds made of natural polymers have proven crucial material design properties for tissue regeneration in biomedical applications [1, 2]. These artificial three-dimensional (3D) platforms must have essential properties when used as medical devices, such as biocompatibility, and in most cases, are bacteriostatic and biodegradable, alongside sufficient mechanical properties [3-5]. An advantage of biopolymer scaffolds compared to synthetic polymers is better cell adherence, enhancing cell viability and spreading [6]. Advanced scaffold fabrication helps create well-defined interconnected micro/nanoscaled pore networks that can mimic aspects of the complex extracellular matrix (ECM) in natural tissues, improving cell ingrowth and nutrient, waste, and oxygen transport [7, 8]. Ideally, biopolymer scaffolds with controlled structural features (e.g., geometry, surface properties, and mechanical performance) could enhance cell-material interaction, guide cell attachment, spreading, and migration, and accelerate skin repair and tissue regeneration [9, 10].

Both porous and non-porous materials are studied for use in tissue engineering. However, porous scaffold-based nanofibers have shown the most promise due to some remarkable features. Nanofibrous scaffolds possess enormous surface-area-to-volume ratio synergy with interconnectivity in a highly porous network similar to the features of natural ECM [11]. Interestingly, nanofibrous structures are controllable depending on specific needs [12]. For example, fiber diameter in the scaffold can be produced well within the range of submicrometer- to micrometer-sized fibers in the fibrillar structure of ECM by controlling the concentration and molecular weight of the polymer [13, 14].

Similarly, fiber morphology (e.g., smooth, porous, aligned, or hollow fibers) can be manipulated by altering spinning parameters (including gas pressure in blow spinning or high voltage in electrospinning, flow rate, tip-to-colletor distance), environmental parameters (temperature and humidity) or using different collector geometries, and co-/tri-axial spinning [15-17]. Scaffolds can serve as gene carriers for regenerative medicine or vehicles for drug delivery. It is feasible to incorporate bioactive compounds, such as wound healing agents, growth factors, and drug agents to meet specific requirements.

Solution blow spinning (SBS) can be applied to produce fibers in a rapid, reproducible, and scalable manner. Compared to electrospinning, SBS offers higher throughput for ensuring a high production yield of fibers with similar diameter ranges [18, 19]. In comparison to electrospinning, no electrical fields are required. The driving force to form fibers is pressurized gas in SBS.

Chitosan was selected due to its well-reported outstanding intrinsic properties (e.g., nontoxicity, bacteriostatic, biocompatibility, and biodegradability), making it one of the most promising materials in tissue engineering [20-23]. The production, chemical structure and properties of chitosan are well described in the literature [24-26]. Owing to the amount of active amino and hydroxyl groups in its polycationic structure, chitosan can be easily modified and effective in binding negatively charged domains (e.g., drugs, polymers, bioactive compounds, DNA, RNA). For example, a norbornene-functionalized chitosan can be a water-soluble derivative while enabling photo-crosslinking, making the polymer stable under physiological conditions [27]. The positive charges of chitosan formed ionic complexes with negative charges on the bacterial cell wall,

disrupting the cell bacteria membrane, altering membrane permeability, inhibiting DNA replication, and subsequently, bacteria cell death [28]. The hemostatic activity can also be related to the positive charges on the chitosan backbone that interact with negatively charged red blood cells [29].

The degree of deacetylation (DDA) of chitosan is an important property that determines its performance of chitosan [30]. Higher DDA chitosan films have been reported to exhibit greater crystallinity, higher elastic modulus, and tensile strength [31]. Surface wettability is also enhanced with increasing DDA [31]. In terms of biological activity, cells on chitosan films of higher DDA adhered better and grew faster than those with low DDA [32, 33]. This can be explained by electrostatic attraction. When the DDA of chitosan increases, the number of positive charges due to the amine group increases, resulting in a stronger interaction with negatively charged molecules, improving mucoadhesive characteristics [34]. As a result, chitosan with higher DDA has been reported to exhibit higher mechanical properties and better cell response.

Electrospinning has been the most used method to produce chitosan/PEO-based fibers. Relatively high concentrations of acetic acid (70–90% v/v in water) or trifluoroacetic acid (99%) have been used to dissolve chitosan, this also increases solution conductivity, making it amenable to the formation of homogenous fiber mats by electrospinning [35-38]. SBS, on the other hand, employs a much more ecologically friendly solvent, i.e., acetic acid aqueous solution at 1–4% (v/v), as the spinning dope and has a greater throughput than conventional electrospinning [39].

The goal of this study was to design and develop a new wound care material in which chitosan nanofibers create a functional outer barrier against bacteria from entering, mimick some aspects of natural skin tissue, and simultaneously provide sufficient mechanical strength to protect the underlying wounded tissue from stress and insult during the healing process. In the present study, we investigate high-throughput nanofiber fabrication applied to highly deacetylated chitosan and demonstrate their desired structure and stability for *in vitro* study and high cellular compatibility.

2. Materials and methods

2.1. Materials

All chemicals were of analytical grade and used as received unless stated otherwise. Chitosan powder with a DDA > 90% (ChitoClear®) was obtained from Primex Ehf (Siglufjordur, Iceland) and characterized in a previous study [40]. Poly(ethylene oxide) (PEO) with a viscosity average molecular weight of 1000 kDa, acetic acid, and potassium carbonate were purchased from Sigma-Aldrich.

Chitosan was dissolved in 0.5M acetic acid at 4 wt% concentration. PEO solutions were prepared at 4 wt% in miliQ-water. All solutions were magnetically stirred in capped vials at room temperature for 24 h to obtain visually homogeneous stock solutions. Chitosan/PEO blend solutions were prepared from these stocks at ratios of 98/2, 95/5, 90/10, 85/15, 70/30, 50/50, and 70/30 by weight. Hereafter, the blended nanofibers produced (described further below) are

referred to by their original blend solution ratios. The solutions were sealed and then stirred for at least 12 h to obtain visually homogeneous solutions. The solutions were kept to rest at room temperature for 1 h prior to solution blow spinning. All solutions were spun and characterized within 48 h of preparation to avoid ageing and degradation effects [41, 42].

2.2. Methods

Solution blow spinning (SBS) of chitosan nanofiber scaffolds

All chitosan/PEO solutions were spun via a custom-made SBS set-up. The apparatus (syringe pump and compressor) and details of the concentric nozzles have been described in the previous work [43]. Chitosan/PEO solutions were loaded into a 10 mL syringes and connected to the SBS head via silicone tubing. The solutions were injected into the inner nozzle at 50 µL/min, with the outer nozzle supplied with pressurized air at 10–14 psi. The inner nozzle tip (internal diameter 0.8 mm) was set to protrude from the outer nozzle by 10 mm. This set-up served to reduce clogging effects. Highest yields of fiber formation were obtained using a hot-air gun (D26960, DeWalt) set at a range 150–200 °C with its nozzle positioned ~ 20 mm distance to the outer nozzle of the SBS emitting head. The SBS fiber emitter and hot-air gun were positioned to point down a glass tube (diameter 60 mm, length 270 mm), which served to channel airflow and guide the fibers to the collector. This set-up acted to force evaporate solvent and facilitated fiber formation and collection. The collector was positioned 100 mm from the end of the glass tube and the total working distance from SBS emitter to collector was 400 mm. The temperature measured at the collector was in the range 45–55 °C. Fibers were collected on a vacuum drum collector (Linari, Italy), rotating at 500 rpm (equivalent to the linear speed 2.09 m/s) and resulted in improved fiber collection compared to a smooth drum. After spinning, the obtained fiber mats were dried in a vacuum oven (VT6025, Thermo Scientific, Germany) at 40 °C for 24 h prior to further characterization. Thermogravimetry analysis (TGA) was conducted to evidence the presence of chitosan and PEO in the obtained fiber mats, as described in the supporting information (SI). Nanofiber mats with 90/10, 80/20, 70/30, and 50/50 chitosan/PEO compositions were selected for further characterization because of their suitable fibrous structure and high chitosan content.

Removal of PEO using a neutralization step

PEO was removed from the fiber mats by immersing as-spun fiber mats into 1M K_2CO_3 aqueous solution (pH 13) for 3 h at room temperature [44]. This enabled the PEO to dissolve and prevented the chitosan from dissolution due to residual acid groups on the fiber surface. In order to prevent shrinkage of the fiber mats during dissolution, the edges of the mats were sandwiched in Teflon frames of dimensions 60 mm (L) x 40 mm (W) and fixed by binder clips. After neutralization, the mats were rinsed thoroughly with milli-Q water until pH 7, followed by drying at room temperature for 24h in an extracted hood and then under vacuum in a desiccator for 24h, remaining at all times in the Teflon frames.

Fiber morphology, diameter and porosity determination

The morphology of the nanofibers was examined using scanning electron microscopy (SEM, TM3030, Hitachi High-Technologies Europe GmbH, Krefeld, Germany). Nanofibers were carefully peeled from the collector, cut into pieces, then mounted on aluminum stubs using double-sided carbon conductive tape, and sputter-coated with gold in 15 s before observing. SEM was conducted on the top surface of the fiber mat, defined as the surface exposed to the air during spinning and used for subsequent cell culture. All images were taken in backscattered electron mode at an accelerating voltage of 15 kV. Using ImageJ software (NIH, USA), fiber diameters were assessed based on 50 fibers per sample type, expressed as mean and standard deviation (SD). The void size between fibers was analyzed in segmented images from original SEM images using ImageJ. The porosity percentage was calculated based on the apparent density of nanofiber mat in comparison with the film [45].

Attenuated total reflectance-Fourier transform infrared (ATR-FTIR) spectroscopy

Functional groups on the nanofiber samples were identified using a PerkinElmer Spectrum 400 equipped with a universal ATR sampler (Perkin Elmer, Waltham, MA, USA). Spectra were recorded at a resolution of 1 cm^{-1} and averaged over 16 measurements to improve the signal-to-noise ratio. The data was processed by a correction for ATR, baseline subtraction, and normalization to the most intense peak at around 1100 cm^{-1} which corresponds to C–O–C stretching vibrations.

Wet and dry fiber mat mechanical property determination

Nanofibrous scaffolds of as-spun and neutralized samples were mechanically tested in tension in dry and wet conditions using a uniaxial testing machine (ZwickiLine, Zwick/Roell Z2.5, Germany) equipped with a 10 N load cell at a strain speed of 0.5 mm/min to failure. A preload of 0.1 N was applied. Test specimens were cut into rectangles with dimensions 30 mm (L) x 5 mm (W) and fixed into card frames (or a Teflon frame for wet conditions) using double side adhesive tapes to ensure the gauge length of 20 mm (L) x 5 mm (W). Wet specimens were prepared by soaking the nanofibers in phosphate buffered saline (PBS) for 30 min at ambient conditions prior to testing. After the specimen was mounted in the machine, the lateral parts of the frames were cut using fine scissors, leaving the fiber free to be tensile tested. The thickness of dry specimens was measured using a digital micrometer (Mitutoyo, Japan) and introduced to the software prior to testing. Three to five specimens were prepared for each nanofiber scaffold type (i.e., 90/10, 80/20, 70/30, 50/50, and neutralized 90/10). Ultimate tensile strength, elongation at break, Young's modulus, and toughness were calculated from stress-strain curves.

***In vitro* cell culture with human dermal fibroblasts**

Normal human dermal fibroblasts (NHDF) (Lonza, Basel, Switzerland) were cultivated in DMEM (Sigma-Aldrich, MO, USA) medium, supplemented with 10% v/v fetal bovine serum (Lonza, NJ, USA), 200 mM GlutaMAX (Thermo Fisher Scientific, MA, USA), 100 U/ml penicillin, and 100 µg/ml

streptomycin (Lonza, NJ, USA) at 37 °C in 5% CO_2 environment. Cells at 80–90% confluency were subcultured using trypsin at a ratio of 1:3, and cells at passage 7 were seeded on the scaffolds.

Chitosan nanofiber scaffolds were mounted onto sterile CellCrown™ 24NX inserts (Scaffdex, Tampere, Finland). The mounted scaffolds were then sterilized in 70% (v/v) ethanol for 30 min, followed by washing in sterile PBS for 30 min, and exposed to UV-light (254 nm) while remaining immersed in the PBS for 20 min prior to cell seeding. NHDF cells were seeded at a density of 5×10^5 cells per well and cultured in DMEM at 37 °C in a 5% CO_2 environment. Cells/scaffolds and media were harvested at days 1, 3, 7, and 14 for further analyses. Media were changed every third day during cell culture. However, in order to ensure the same window of protein secretion and cellular exposure to new media, an additional media change was performed 24 h prior to harvesting at days 3, 7, and 14. Cells were also seeded on glass coverslips (MultiSlip™ inserts 12 mm (L) x 12 mm (W), Sigma-Aldrich, Germany) as control samples in 24 well plates to follow cell number and morphology.

Lactate dehydrogenase (LDH) activity

Cytotoxic effects of the nanofiber scaffolds were evaluated by the LDH activity in the collected cell culture media at days 1, 3, 7, and 14 using a cytotoxicity detection kit (Roche Diagnostics, Mannheim, Germany). Duplicates of 100 µL of the sample were added to 100 µL of a mixture (catalyst and dye solution) and incubated at 25 °C in the dark for 30 min before measuring the absorbance at a wavelength of 450 nm, according to the manufacturer's kit instructions. The absorbance was read using a microplate reader (ELx800™, Bio-Tek Instruments Inc., VT, USA). The data obtained were expressed relative to control.

Confocal imaging of cell and fibrous morphology

Harvested scaffolds were fixed with 4% w/v paraformaldehyde for 30 min and washed in PBS three times. Cells were stained with DRAQ5 and Alexa Fluor™ 594 Conjugate wheat germ agglutinin (WGA) (Invitrogen, CA, USA) to label cell nuclei and cell membranes. Alternatively, cells were permeabilized with 0.1% Triton X-100 for 5 minutes, washed with PBS, and stained with DRAQ5 and phalloidin-Alexa Fluor 568 to label nuclei and actin cytoskeleton. Immunofluorescence stained samples were observed under a confocal fluorescence microscope (Leica TCS SP8, Leica Microsystems CMS GmbH, Germany) with 10x/0.40 dry and 20x/0.50 water immersion objective lenses. Excitation and bandpass emission wavelengths were 552 nm and 580–625 nm (Alexa Fluor 568), 552 nm and 600–645 nm (Alexa Fluor 594), and 638 nm and 670–750 nm (DRAQ5). Autofluorescence of chitosan fibers was observed at an excitation wavelength of 488 nm with bandpass emission filters set to 500–550 nm and enabled imaging of the fibers. Images were scanned as z-stacks using sequential scanning with the pinhole set to 2 airy units and processed to maximal projections using FIJI [46].

Quantification of secreted proteins in cell culture medium

Specific proteins secreted by the fibroblasts to the cell culture medium were quantified using the Milliplex Human Sepsis Magnetic Bead Panel 3 - Immune Response Multiplex Assay (HSP3MAG-63K; Elastase-2, lipocalin-2/neutrophil gelatinase-associated lipocalin (NGAL), thrombospondin-1) and Human Adipocyte Magnetic Bead Panel - Endocrine Multiplex Assay (HADCYMAG-61K; Interleukin 6 (IL-6), leptin, interleukin 8 (IL-8), hepatocyte growth factor (HGF), adiponectin, monocyte chemoattractant protein-1 (MCP-1), tumor necrosis factor (TNFα), resistin) (Millipore Merck, MA, USA). All analyses were performed according to the manufacturer's protocols. A Luminex 200 system with xMAP technology (Luminex, TX, USA) was employed for the multi-analyte profiling of the protein levels in cell culture media, which were previously collected after 1, 3, 7, and 14 days of culture. Acquired fluorescence data were analyzed by the xPONENT® 3.1 software (Luminex, TX, USA).

Statistical analysis

Statistical analysis was performed using OriginPro® 2020 (OriginLab, USA) or SigmaPlot 14.0 (Systat Software Inc., USA). Statistical significance between different groups was analyzed by one-way analysis of variance (ANOVA). After ANOVA, Tukey's post hoc test was used for comparison. The significance level was set to $p \leq 0.05$.

3. Results and discussion

3.1. Optimization of chitosan nanofiber blow spinning

Spinning neat chitosan into nanofibers is challenging due to the structural rigidity of chitosan and its propensity to form specific inter and intra-molecular hydrogen bonds [38, 47]. PEO is commonly added as a spinning aid to improve chain entanglement and form hydrogen bonds between the hydroxyl and amino groups on chitosan chains with ether groups in PEO [48, 49].

The concentrations of chitosan and acetic solvent are some of the primary factors affecting its spinnability via the SBS process. The concentration of chitosan solution and choice of acidic solvent govern spinnability in solution blow spinning. Solution viscosity can be altered readily and changing acetic acid concentration can alter surface tension [14]. Initial SBS experiments indicate that chitosan nanofiber formation was relatively feasible at a concentration of acetic acid 50–90 wt% (data not shown). This agrees with previous reports in the literature, where concentrated acetic acid has been used as a solvent for chitosan to obtain bead-free fibers using electrospinning [35, 36]. Drawbacks to using highly concentrated acids include downstream removal issues for cell culture. Dilute aqueous acidic solution (2 wt% concentration) was used for chitosan spinning dope formulation hereafter in this work. Concentrations of chitosan solution $>$ 4 wt% resulted in difficulties in SBS due to increased viscosity, whereas concentrations < 2 wt% resulted in significant droplet deposition in the nanofibrous mats, local dissolution, and film formation [14, 50]. Consequently, chitosan was dissolved at 4 wt% in 2 wt% aqueous acetic acid and mixed with an aqueous solution of PEO at 4 wt% at different blend ratios compositions for the blow spinning process.

The morphology of the obtained nanofibers is shown in Figure 1. Fiber formation was facile for chitosan samples containing high PEO content. Indeed, chitosan nanofibers consisting of 10–50 wt% PEO appear as homogeneous fibers with a near defect-free fibrous network. On the contrary, regions of film formation and fused fibers are evident from the sample with the lowest PEO (the 98/2 sample, Figure 1A), likely due to droplets hitting the mat in process, and there is evidence of bead formation in the 95/5 sample, Figure 1B. The presence of chitosan in the chitosan/PEO nanofibers and interactions between PEO and chitosan was assessed by ATR-FTIR and summarized in Figure 2. ATR-FTIR spectra for chitosan/PEO blend nanofibers, neat chitosan and PEO solution-cast films were prepared with the same solvents as those used in the SBS process.

Almost all spectra of PEO are overlapped with those of chitosan. Neat PEO exhibits a typical absorption band at 2874 cm^{-1} due to CH_2 stretching (Figure 2A). However, this band overlapped with that detected for the neat chitosan sample and all blend compositions. Other characteristic bands of PEO are observed at 1465 cm^{-1} assigned to C–H bending, at 1341, 1280, and 1240 cm^{-1} assigned to C–H deformation of the methyl group, at 1097, 961, and 841 cm^{-1} assigned to C–O–C stretching vibrations [51].

Neat chitosan and all compositions exhibit broad bands at 3600–3000 cm^{-1} (Figure 2A), attributed to NH and OH groups [52]. Due to added PEO, intensity changes and slightly shifted peaks at some absorption bands indicate the interaction between chitosan and PEO. For example, a shoulder band at 1632 cm^{-1} of pure chitosan shifted to 1652 cm^{-1} for all blend compositions (Figure 2B). This corresponds to C=O stretching in the *N*-acetyl groups (NH–RC=O, known as amide I) and is also evidence of acetyl residual from the deacetylation process of chitosan [53]. The band at 1561 cm^{-1} assigns to the N–H bending in the primary amide (amide II) NH_2 absorption band. The band at 1406 cm^{-1} can be attributed to either the C–N stretching of primary amide (amide III) or deformation of the CH_3 vibration [54]. The other bands in the range 1200–600 cm^{-1} can be assigned to the stretching vibrations of the C–O–C bridge [55] or characteristics of the polysaccharide structure of chitosan [52].

There is a possibility of ammonium (NH_3^+) ion accumulation in neat chitosan and all its blend compositions due to the protonation of $–NH_2$ caused by acetic acid. The absorption bands, which correspond to the $N–H^+$ stretching vibrations (3350–3100 cm^{-1}) and deformation vibrations (1635–1480 cm^{-1}), are seen and overlapped with characteristic bands for chitosan in the same region [56].

3.2. Fiber diameter and porosity in the fiber networks

In the design of biomaterials that mimic aspects of the mechanical properties of the epidermis, fiber network structure is important to characterize. This is in addition to other requirements such as biocompatibility and bioactivity [57]. Fiber diameter, fiber network density, alignment, waviness, and network points (e.g., crosslinks) impact mechanical behavior, and porosity and interfiber void space influence cell attachment and migration.

Fiber diameters significantly increase with increasing the PEO content (summarized in Figure 3A), ranging from 270 ± 46 nm to 1057 ± 231 nm. A more narrow distribution of fiber diameter was observed for low PEO content chitosan nanofibers. These had an average diameter of 265 nm versus 1300 nm for neat PEO fibers (data not shown). The fiber diameter followed an increasing trend concomitant with increased PEO loading. Porosity showed a percentage of around 30-60% for 95/5, 90/10, 80/20, 70/30, and 50/50 chitosan/PEO nanofibers (Figure 3A), which is in connection with the void sizes of 150–500 nm (Figure 3B). Nanofiber mats from the 50/50 composition had a large void but a low porosity percentage (around 40%). This might be due to the dense fibrous network containing 50% of the PEO spinning aid, which contributes to thick and thin fibers, better covering the void volume between fibers in the whole fiber mat and decreasing porosity. The evidence of thick and thin fibers in the 50/50 composition is associated with the largest fiber diameter distribution (SD = 250 nm) than any other composition. The highest porosity (75%) and largest void (700 nm) seen in the 30/70 nanofiber mat suggested the increasing trend of these parameters in association with fiber diameter, in agreement with other reports in the literature [58].

It is known that a scaffold with high porosity and a large void can favor cell ingrowth [59]. For example, a silk fibroin scaffold with 86% porosity and void sizes of 200–250 μm enabled better human foreskin fibroblast proliferation [60]. However, there is always a balance between porosity and mechanical properties in the design of promising scaffolds, as high porosity yields lower mechanical strength. The dense fibrous network with high porosity in synergy with sufficient mechanical properties (discussed in section 3.4) in this study may be suitably applied as the top layer in designing a multigradient skin scaffold [57].

Native collagen fibrils in tissues are in the range of 50–500 nm [61]. Chitosan/PEO fibers with < 10 % PEO content fall in this range, having a mean diameter of 420 nm. This composition was selected for further characterization and *in vitro* studies due to fibrous structure and high chitosan content, known for antibacterial properties [62].

3.3. Neutralization step and removal of PEO in chitosan nanofibers

When chitosan/PEO nanofibers are immersed in water, they are swollen because both chitosan and PEO are unstable or progressively solubilized in water, leading to structural changes and changes in their properties and morphology. In order to obtain a more stable chitosan fiber network, a neutralization and PEO dissolution step was taken[63, 64]. In this study, the main advantages of neutralization are converting protonated amine groups ($-NH_3^+$) to the $-NH_2$ form, thereby making the fiber insoluble in aqueous media while simultaneously solvating and removing the PEO from the nanofibers.

The fibrous structure of the neutralized sample is integrally preserved after 3 h soaking in K_2CO_3 (Figure 4), even after continuous immersion in cell culture media (PBS, pH = 7.4) for 14 days. There is some evidence of fusion and conjoining between fibers structure, which leads to fiber size increment (mean diameter of 439 nm for as-spun 90/10 increases to 571 nm for neutralized

90/10). This could also be due to some deformation of round section fibers to ribbon-like structures. This change can be explained both by the hydration of protonated chitosan fiber when it first contacts water or the swelling of the PEO residue [63]. Compared to previous studies, the fibrous structural integrity maintained after neutralization in this study is superior for cell culture since fiber did not undergo a significant fusion caused by chemical crosslinking [35, 65] or other neutralization methods [44, 63].

As discussed in the FTIR result section, the presence of $-NH_3^+$ on the nanofibers is detected, therefore conversion to the $-NH_2$ group is expected after neutralization. However, due to the overlapping bands between amide II and $-NH_3^+$, only the decrease in intensity and peak shift are observed at around 1558 cm^{-1} in the neutralized sample (see ATR-FTIR results in Figure S2A).

The neutralization step also resulted in effective PEO removal. NMR was conducted to investigate chemical changes of the neutralized nanofibers, as described in the supporting information. Indeed, the ratio of proton integral of the $-CH_2-$ group in PEO (chemical shifts $\sim$ 3.58 ppm) and in chitosan (chemical shifts $\sim$ 3.08 ppm) for the neutralized 90/10 is suppressed drastically in comparison to the same ratio for as-spun 90/10 (see NMR results in Figure S2B). The result agrees with a previous study [44], and indicates that PEO was extracted from the chitosan nanofibers after neutralization.

3.4. Mechanical properties determined in dry/wet states

Appropriate mechanical durability of nanofiber scaffolds is crucial in skin tissue engineering because those skin substitute materials should withstand an applied load and demonstrate fast recovery in the same order of magnitude as skin tissues [66]. Ideally, they would be able to mimic the skin elasticity.

The mechanical properties of the chitosan/PEO nanofibers assessed in the dry and wet states are shown in Figure 5 (all compositions, non-neutralized) and Figure 6 (neutralized). Ultimate tensile strength (UTS), elongation at break, Young's modulus, and toughness are summarized in Tables 1 and 2. As seen in Figure 5, UTS significantly increases for fiber scaffolds containing high content of PEO, especially at sample having 50% PEO (i.e., 50/50), the highest value of 17.13 $\pm$ 3.73 MPa is obtained. This sample also exhibits maximum elongation at break. These results imply that adding PEO enhances fiber strength, strain to failure, and toughness. This is likely due to strong interactions caused by new hydrogen bonds that formed between hydrogen atoms of hydroxyl and amino groups on chitosan molecules and ether oxygen of PEO [67].In addition, there was no significant difference in Young's modulus observed at all compositions, except 90/10 with a slightly lower value of 2.97 $\pm$ 0.47 MPa.

In comparison to literature studies, the UTS of Chitosan/PEO nanofibers in this work is close to that of chitosan/PEO (90/10) containing (0-2 wt%) henna extracts, which was reported in the range 7.2–13.3 MPa, while our elongation at break is lower [68]. A similar UTS value (7.5 MPa) was reported for chitosan/PEO (95/5) nanofibers, albeit with a much lower elongation at break

(0.05%) [69]. In contrast, our tested scaffolds in wet conditions (described below) demonstrate a significant improvement in mechanical properties, whereas UTS dropped two to three times and elongation at break remained nearly constant in their works [68, 69].

Table 1. Ultimate tensile strength, elongation at break, Young's modulus, and toughness of as-spun chitosan/PEO nanofiber scaffolds

Chitosan/PEO	Ultimate tensile strength (MPa)	Elongation at break (%)	Young's modulus (MPa)	Toughness (MJ/m^3)
90/10	7.42 ± 2.19	3.73 ± 1.05	2.97 ± 0.47	0.08 ± 0.03
80/20	$14.36 \pm 2.02^{(*)}$	5.57 ± 1.32	$5.86 \pm 0.39^{(*)}$	0.56 ± 0.23
70/30	11.14 ± 0.10	$9.55 \pm 3.41^{(*)}$	$5.12 \pm 0.40^{(*)}$	0.72 ± 0.27
50/50	$17.13 \pm 3.73^{(*)}$	$17.38 \pm 2.38^{(*)}$	4.54 ± 1.26	$1.70 \pm 0.58^{(*)}$

Data are representative of three to five independent experiments and represented as mean $\pm$ SD.$^{(*)}$ denotes statistically significant differences against 90/10 ($p < 0.05$).

The 90/10 sample was down-selected for *in vitro* studies, and mechanical properties followed in the as-made state (dry) and following neutralization (both wet and dry state). The membrane must retain sufficient mechanical stability to undergo cell culture. The mechanical properties of as-spun 90/10, neutralized 90/10 dry, and neutralized 90/10 samples in the wet state are shown in Figure 6. After neutralization treatment, the dry scaffold becomes rigid and brittle as UTS and Young's modulus increase almost double that of the as-spun scaffold. This can be explained by the successfully removing PEO, which otherwise acts as a plasticizer in the scaffold. A significant difference is seen for the neutralized nanofiber scaffold in the wet state. The wet scaffold undergoes significant strain to failure, approaching 30% (Table 2). However, its UTS is slightly lower than that of neutralized dry scaffold but the elongation at break significantly increases up to 44% of its original length. In company with the lowest Young's modulus, the wet scaffold is proven as a tough scaffold having notable strength, elasticity, and plasticity. SEM assessed the different morphologies of the fracture surfaces of these scaffolds (Figure 6B–E). After fracture, the fibrous structure of the neutralized wet scaffold exhibits integral stability with wavy fibers near the breaking line (Figure 6C) and straight fibers in other areas of the specimen (Figure 6D). In the neutralized dry specimen, straight fibers are seen dominant surrounding the fracture site (Figure 6E).

Table 2. Ultimate tensile strength, elongation at break, Young's modulus, and toughness of the as-spun, neutralized dry, and neutralized wet chitosan/PEO (90/10) nanofiber scaffolds

Chitosan/PEO (90/10)	Ultimate tensile strength (MPa)	Elongation at break (%)	Young's modulus (MPa)	Toughness (MJ/m^3)
As-spun	7.42 ± 2.19	$3.73 \pm 1.05^{(**)}$	$2.97 \pm 0.47^{(**)}$	$0.08 \pm 0.03^{(*)}$
Neutralized dry	18.46 ± 3.57	11.15 ± 5.00	$7.04 \pm 1.44^{(***)}$	1.47 ± 0.92
Neutralized wet	13.08 ± 4.40	28.87 ± 14.96	0.25 ± 0.06	1.57 ± 0.68

Data are representative of three to five independent experiments and represented as mean ± SD. (*) (**) and (***) denote statistically significant differences against neutralized wet sample ($p <$ 0.05, 0.01, and 0.001, respectively).

The mechanical properties of chitosan nanofiber scaffolds in this work can be compared to two of the major components in soft tissues of human skin, collagen and elastin [66]. Specifically, comparing our data to that of human skin in the literature, the strength of dry/wet chitosan nanofiber scaffolds far exceeds that of excised full-thickness skin of an 85-year-old male (3 ± 1.5 MPa) [70]. In another skin study carried out at age 81–97, the data in this work fall within values of 21.6 ± 8.4 MPa (UTS), 54 ± 17% (elongation at break), and 1.18 ± 0.88 MPa (Young's modulus) [71]. Therefore, the results demonstrate that the scaffolds in this study could be potentially used as skin substitutes.

3.5. *In vitro* cell culture

3.5.1. Cytotoxicity and confocal imaging of cell-nanofiber scaffolds

Following the neutralization process and the initial characterization of the nanofiber scaffolds, *in vitro* tests were conducted to examine the cellular interactions with the scaffolds. Since fibroblasts are the most abundant cells in various tissues and play a key role in wound healing, angiogenesis, and tissue regeneration [72], we used NHDF cells to investigate the cytocompatibility of chitosan nanofiber scaffolds.

The effect of two types of neutralized scaffolds containing different chitosan densities (90/10 (higher) and 50/50 (lesser)) on NHDF cell behavior was examined after 1, 3, 7, and 14 days. As seen in Figure 7, there is no statistical difference ($p > 0.05$) in the LDH activity between the time points tested within each group (90/10 and 50/50). A higher LDH activity is found for 90/10 at days 3 and 14, indicating that more cells are vital in the group 50/50 compared to the group 90/10, however, there was no significant difference.

The morphologies of cells seeded on fiber scaffolds are visualized in fluorescence and SEM images, as seen in Figure 8. A clear organization of cell nuclei and membranes is seen in control cells cultured on glass coverslip inserts while significant differences in the cell morphology are seen between the two scaffolds. On the 2D flat, hard glass surface, cells exhibit a tetrahedral morphology, however the neutralized 90/10 scaffold shows cell adhesion with high spreading of cells, and the cells have stretched structures with a spindle-shape. During the 14-day cell culture period, the cells on the 90/10 scaffold align, forming groups that orientate in a particular direction. This may indicate that the cells have established the focal adhesive points onto the fiber surface, allowing them to spread [73].

Morphology of cell-nanofiber contacts is given by SEM images (Figure 8). The cells exhibit flattened morphology on the surface of fiber scaffolds at all time points, alongside the details of retained fibrous structure, exhibiting more flexural fibers after long-term culture. Although the fiber scaffolds are isotropically anchored in the cell crown, their lengthy exposure to the cell

medium may have created surface tension at the subcellular level, i.e., aligned fibers induced by wet conditions. As a result, nanofibers are locally oriented, thus guiding the cell adhesion along one direction. Moreover, as evidenced in the fluorescence image on day 14, cells are aligned due to stretched fibers while in the SEM photo, flexural fibers are seen when surface tension is released by drying.

On the other hand, in the 50/50 scaffold samples, there appear to be limited numbers of cells adhering to the scaffold, and the cells are rounded and aggregated in close, compact structures. Almost no cell interaction with surrounding fiber matrices is observed for any of the time points tested. Longer culturing time results in larger aggregates of cells, yet a relatively small number of cell aggregates are seen.

Thus far, the larger cell areas and extensively stretched cell bodies found in 90/10 signify a more preferred scaffold for cell attachment than the 50/50 scaffold. This indicates better cytocompatibility of the higher chitosan fiber scaffold, promoting cell adhesion and survival. It is, however, noted that the cells did not appear to be apparently distributed over the whole fiber surfaces as in the controls. One explanation may be a non-uniform charge distribution at the surface of chitosan fibers due to neutralization [65]. Further improved cell adhesion to chitosan scaffolds might be achieved by functionalizing chitosan fiber surface by grafting with poly(lactic acid) [74] or coating with laminin or fibronectin [37, 75], or blending with other polymers and bioactive compounds to obtain multilayer scaffolds [76].

Another significant aspect found during confocal imaging is the noticeable autofluorescent characteristic of chitosan fibers. As seen in Figure 9A, the fluorescence merged image clearly visualizes cell density and cell-nanofiber details that are difficult to see in the bright field SEM image (Figure 9E). Individual fluorescence labeling demonstrates cell nuclei (here presented in the blue channel, Figure 9B) and cell membranes (Figure 9C, magenta channel), and simultaneously, the intense green fluorescence of chitosan nanofibers (λ_{em} = 515 nm). This striking property would help visualize more complex structures based on chitosan for *in vitro/in vivo* staining. Although the autofluorescence of chitosan has been demonstrated previously [65, 77, 78], none of them has mentioned the advantage of combining scaffold autofluorescence with specific cell staining to visualize the sample as a whole.

The mechanism of cell-scaffold interaction is not the aim for this work, however the penetration of cells into the fiber scaffold is noticed in the SEM photo (Figure 9E). Some fibers are evidently visible at the surface of the cell spreading regions which are indicated by red arrows. Infiltration of cells into the matrix was also noted during scanning of z-stacks with confocal microscopy, however this cannot be represented in the maximal projections images shown here. Orthogonal plane projection of the confocal 3D image stacks may be used to verify infiltration of cells into the scaffold, however, due to scattering within the specimen and the reduced *z* resolution inherent in confocal microscopy, the quality of the images failed to support this to a sufficient degree. Therefore, a comprehensive investigation of cell infiltration requires more experimental trials.

3.5.2. Secreted proteins to the culture medium

Multiple secreted proteins, including cytokines, chemokines, and growth factors that play roles in wound healing application, were quantified in the medium from fibroblasts cultured on the neutralized 90/10 scaffold. Most of the selected factors (Elastase-2, NGAL, thrombospondin-1, leptin, adiponectin, resistin, and TNFα) had concentrations below the detection limit or the standard curve for the assays. Figure 10 shows the secreted levels of IL-6, IL-8, HGF, and MCP-1 proteins in the cell culture media on days 1, 3, 7, and 14.

IL-6 plays a central role in acute inflammation and is necessary for the resolution stages of wound healing [79]. The secretion of IL-6 is found to enhance over time. It is worth noting that IL-6 secretion on day 1 is much higher than that of the control group (same number of cells seeded on glass coverslips). IL-8, produced by fibroblasts residing in injured local tissues, is one of the well-known chemokines [80]. Moreover, secretion amount of IL-8 follows the same increasing trend as IL-6 in culture time.

HGF plays a facilitating role in the healing process of the corneal epithelium in the form of paracrine secretion [81]. It has been found to stimulate epithelial and endothelial cell proliferation, motility, and morphogenesis. HGF is recognized as a potent anti-inflammatory and anti-fibrotic growth factor [82] and may induce angiogenesis in many organs, which is critical in wound healing. The secretion rate of HGF increases on days 1–7, and maintains a relatively stable secretion rate until day 14, indicating that it may benefit the healing of skin wounds.

MCP-1 participates in the recruitment of monocytes during wound healing, which differentiates into M1 macrophages with the participation of a variety of cytokines [83]. MCP-1 has also been recognized as an angiogenic chemokine [84]. Secretion of MCP-1 shows the highest value on day 3 and a slight decrease on days 7 and 14.

Taken together, the wound healing-related protein secretion profiles demonstrate that the neutralized 90/10 scaffold is a suitable platform for cell migration and may promote the wound healing process.

4. Conclusions

High-throughput technique, solution blow spinning, has been used to form chitosan/PEO blend nanofiber scaffolds using chitosan with a degree of deacetylation > 90%. PEO presence in chitosan solutions facilitated the spinning process, producing fine fibers with diameters of 300–1200 nm and a 30–75% porosity. Chitosan/PEO nanofibers with 10% PEO content were down-selected for mechanical testings and *in vitro* studies since they exhibited a favorable balance of ultrafine fibrous structure and high chitosan content. Prior to testing, PEO was removed using a neutralization step in an effort to preserve the fibrillar morphology. Treatment in aqueous potassium carbonate solution maintained fibrous structural integrity and permitted PEO removal. Proof-of-concept mechanical testings of chitosan scaffolds in the dry and wet states proved their strength and toughness were significant and should be sufficient for wound dressing

applications. Interestingly, the wet scaffold was found to have notable strength, strain to failure, and toughness in combination with fibrous structural integrity. *In vitro* studies confirmed that the scaffolds spun from a high chitosan content blend solution were compatible with NHDF cells, indicating a suitable platform for cell adhesion, viability, and proliferation. Secretion of proteins to the cell culture medium from NHDF cells cultured on chitosan fiber scaffolds indicated that this might be a promising scaffold for wound healing. The striking autofluorescent characteristic of chitosan fibers was found to help advance visualizing more complex structures based on chitosan for *in vitro/in vivo* staining. These properties could adapt to and protect skin tissue under stress and pave the way for the new designs and fabrication of novel materials for skin substitutes and dermal tissue engineering.

CRediT authorship contribution statement

Nguyen D. Tien: Conceptualization, Methodology, Formal analysis, Investigation, Writing – original draft, Writing – review & editing. **Tianxiang Geng**: Methodology, Formal analysis, Writing – review & editing. **Catherine A. Heyward**: Methodology, Formal analysis, Writing – review & editing. **Janne E. Reseland**: Supervision, Writing – review & editing. **Jonny J. Blaker**: Conceptualization, Supervision, Funding acquisition, Writing – review & editing. **S. Petter Lyngstadaas**: Conceptualization, Supervision, Funding acquisition, Writing – review & editing. **Håvard J. Haugen**: Conceptualization, Supervision, Funding acquisition, Writing – review & editing.

Declaration of competing interest

The authors declare no competing financial interest.

Acknowledgments

This work was funded by the project “A Bioactivated Nanolayered Hydrogel for Dermal Regeneration in Hard-to-Heal Ulcers” with the acronym BioNaNOR funded by Research Council of Norwegian (RCN) Nano2021 grant number 287991”. The authors thank Dr. Claudio Montier (University of Aveiro) and Ms. Yiru Huo (University of Manchester) for the help of TGA and discussion on the solution blow spinning set-up.

Appendix A. Supplementary data

Supplementary material

References

[1] R.S. Ambekar, B. Kandasubramanian, Progress in the Advancement of Porous Biopolymer Scaffold: Tissue Engineering Application, Industrial & Engineering Chemistry Research 58(16) (2019) 6163-6194.
[2] S. Van Vlierberghe, P. Dubruel, E. Schacht, Biopolymer-Based Hydrogels As Scaffolds for Tissue Engineering Applications: A Review, Biomacromolecules 12(5) (2011) 1387-1408.
[3] A. Kirillova, T.R. Yeazel, D. Asheghali, S.R. Petersen, S. Dort, K. Gall, M.L. Becker, Fabrication of Biomedical Scaffolds Using Biodegradable Polymers, Chemical Reviews (2021).

[4] N. Monteiro, M. Martins, A. Martins, N.A. Fonseca, J.N. Moreira, R.L. Reis, N.M. Neves, Antibacterial activity of chitosan nanofiber meshes with liposomes immobilized releasing gentamicin, Acta Biomaterialia 18 (2015) 196-205.
[5] M. Rahmati, E.A. Silva, J.E. Reseland, A.H. C, H.J. Haugen, Biological responses to physicochemical properties of biomaterial surface, Chem Soc Rev 49(15) (2020) 5178-5224.
[6] M.S.B. Reddy, D. Ponnamma, R. Choudhary, K.K. Sadasivuni, A Comparative Review of Natural and Synthetic Biopolymer Composite Scaffolds, Polymers 13(7) (2021) 1105.
[7] A.M. George, S.P. Reddy Peddireddy, G. Thakur, F.C. Rodrigues, Chapter 29 - Biopolymer-based scaffolds: Development and biomedical applications, in: K. Pal, I. Banerjee, P. Sarkar, D. Kim, W.-P. Deng, N.K. Dubey, K. Majumder (Eds.), Biopolymer-Based Formulations, Elsevier2020, pp. 717-749.
[8] S. Chen, J.V. John, A. McCarthy, J. Xie, New forms of electrospun nanofiber materials for biomedical applications, Journal of Materials Chemistry B 8(17) (2020) 3733-3746.
[9] C.-C. Xue, M.-H. Li, L. Sutrisno, B.-B. Yan, Y. Zhao, Y. Hu, K.-Y. Cai, Y. Zhao, S.-H. Yu, Z. Luo, Bioresorbable Scaffolds with Biocatalytic Chemotherapy and In Situ Microenvironment Modulation for Postoperative Tissue Repair, Advanced Functional Materials 31(20) (2021) 2008732.
[10] F.V. Ferreira, C.G. Otoni, K.J. De France, H.S. Barud, L.M.F. Lona, E.D. Cranston, O.J. Rojas, Porous nanocellulose gels and foams: Breakthrough status in the development of scaffolds for tissue engineering, Materials Today 37 (2020) 126-141.
[11] X. Wang, B. Ding, B. Li, Biomimetic electrospun nanofibrous structures for tissue engineering, Materials Today 16(6) (2013) 229-241.
[12] J. Xue, T. Wu, Y. Dai, Y. Xia, Electrospinning and Electrospun Nanofibers: Methods, Materials, and Applications, Chemical Reviews 119(8) (2019) 5298-5415.
[13] H. Homayoni, S.A.H. Ravandi, M. Valizadeh, Electrospinning of chitosan nanofibers: Processing optimization, Carbohydrate Polymers 77(3) (2009) 656-661.
[14] X. Geng, O.-H. Kwon, J. Jang, Electrospinning of chitosan dissolved in concentrated acetic acid solution, Biomaterials 26(27) (2005) 5427-5432.
[15] P.K. Szewczyk, U. Stachewicz, The impact of relative humidity on electrospun polymer fibers: From structural changes to fiber morphology, Advances in Colloid and Interface Science 286 (2020) 102315.
[16] M. Toriello, M. Afsari, H.K. Shon, L.D. Tijing, Progress on the Fabrication and Application of Electrospun Nanofiber Composites, Membranes 10(9) (2020) 204.
[17] J. Yoon, H.-S. Yang, B.-S. Lee, W.-R. Yu, Recent Progress in Coaxial Electrospinning: New Parameters, Various Structures, and Wide Applications, Advanced Materials 30(42) (2018) 1704765.
[18] J. Song, Z. Li, H. Wu, Blowspinning: A New Choice for Nanofibers, ACS Applied Materials & Interfaces 12(30) (2020) 33447-33464.
[19] J.L. Daristotle, A.M. Behrens, A.D. Sandler, P. Kofinas, A Review of the Fundamental Principles and Applications of Solution Blow Spinning, ACS Applied Materials & Interfaces 8(51) (2016) 34951-34963.
[20] P. Sahariah, M. Másson, Antimicrobial Chitosan and Chitosan Derivatives: A Review of the Structure–Activity Relationship, Biomacromolecules 18(11) (2017) 3846-3868.
[21] M. Hosseinnejad, S.M. Jafari, Evaluation of different factors affecting antimicrobial properties of chitosan, International Journal of Biological Macromolecules 85 (2016) 467-475.
[22] R. Jayakumar, M. Prabaharan, P.T. Sudheesh Kumar, S.V. Nair, H. Tamura, Biomaterials based on chitin and chitosan in wound dressing applications, Biotechnology Advances 29(3) (2011) 322-337.
[23] N.M. Alves, J.F. Mano, Chitosan derivatives obtained by chemical modifications for biomedical and environmental applications, International Journal of Biological Macromolecules 43(5) (2008) 401-414.
[24] N.D. Tien, S.P. Lyngstadaas, J.F. Mano, J.J. Blaker, H.J. Haugen, Recent Developments in Chitosan-Based Micro/Nanofibers for Sustainable Food Packaging, Smart Textiles, Cosmeceuticals, and Biomedical Applications, Molecules 26(9) (2021).

[25] M. Másson, Chapter 33 - Chitin and chitosan, in: G.O. Phillips, P.A. Williams (Eds.), Handbook of Hydrocolloids (Third Edition), Woodhead Publishing2021, pp. 1039-1072.
[26] J.A. Jennings, J.D. Bumgardner, Chitosan Based Biomaterials Volume 1: Fundamentals, Woodhead Publishing2016.
[27] S.E.S. Michel, F. Dutertre, M.L. Denbow, M.C. Galan, W.H. Briscoe, Facile Synthesis of Chitosan-Based Hydrogels and Microgels through Thiol–Ene Photoclick Cross-Linking, ACS Applied Bio Materials 2(8) (2019) 3257-3268.
[28] H. Yilmaz Atay, Antibacterial Activity of Chitosan-Based Systems, Functional Chitosan (2020) 457-489.
[29] S.B. Rao, C.P. Sharma, Use of chitosan as a biomaterial: Studies on its safety and hemostatic potential, Journal of Biomedical Materials Research 34(1) (1997) 21-28.
[30] S. Bhardwaj, N.K. Bhardwaj, Y.S. Negi, Effect of degree of deacetylation of chitosan on its performance as surface application chemical for paper-based packaging, Cellulose 27(9) (2020) 5337-5352.
[31] L.J.R. Foster, S. Ho, J. Hook, M. Basuki, H. Marçal, Chitosan as a Biomaterial: Influence of Degree of Deacetylation on Its Physiochemical, Material and Biological Properties, PLOS ONE 10(8) (2015) e0135153.
[32] C. Wenling, J. Duohui, L. Jiamou, G. Yandao, Z. Nanming, Z. Xiufang, Effects of the Degree of Deacetylation on the Physicochemical Properties and Schwann Cell Affinity of Chitosan Films, Journal of Biomaterials Applications 20(2) (2005) 157-177.
[33] C. Chatelet, O. Damour, A. Domard, Influence of the degree of acetylation on some biological properties of chitosan films, Biomaterials 22(3) (2001) 261-268.
[34] P. He, S.S. Davis, L. Illum, In vitro evaluation of the mucoadhesive properties of chitosan microspheres, International Journal of Pharmaceutics 166(1) (1998) 75-88.
[35] P. Kianfar, A. Vitale, S. Dalle Vacche, R. Bongiovanni, Photo-crosslinking of chitosan/poly(ethylene oxide) electrospun nanofibers, Carbohydrate Polymers 217 (2019) 144-151.
[36] P. Bösiger, I.M.T. Richard, L. Le Gat, B. Michen, M. Schubert, R.M. Rossi, G. Fortunato, Application of response surface methodology to tailor the surface chemistry of electrospun chitosan-poly(ethylene oxide) fibers, Carbohydrate Polymers 186 (2018) 122-131.
[37] D.M. Ridolfi, A.P. Lemes, S. de Oliveira, G.Z. Justo, M.V. Palladino, N. Durán, Electrospun poly(ethylene oxide)/chitosan nanofibers with cellulose nanocrystals as support for cell culture of 3T3 fibroblasts, Cellulose 24(8) (2017) 3353-3365.
[38] K. Ohkawa, D. Cha, H. Kim, A. Nishida, H. Yamamoto, Electrospinning of Chitosan, Macromolecular Rapid Communications 25(18) (2004) 1600-1605.
[39] W. Han, S. Xie, X. Sun, X. Wang, Z. Yan, Optimization of airflow field via solution blowing for chitosan/PEO nanofiber formation, Fibers and Polymers 18(8) (2017) 1554-1560.
[40] M. Sukul, P. Sahariah, H.L. Lauzon, J. Borges, M. Másson, J.F. Mano, H.J. Haugen, J.E. Reseland, In vitro biological response of human osteoblasts in 3D chitosan sponges with controlled degree of deacetylation and molecular weight, Carbohydrate Polymers 254 (2021) 117434.
[41] R.R. Klossner, H.A. Queen, A.J. Coughlin, W.E. Krause, Correlation of Chitosan's Rheological Properties and Its Ability to Electrospin, Biomacromolecules 9(10) (2008) 2947-2953.
[42] A.V. Mironov, G.A. Vikhoreva, N.R. Kil'deeva, S.A. Uspenskii, Reasons for unstable viscous properties of chitosan solutions in acetic acid, Polymer Science Series B 49(1) (2007) 15-17.
[43] A. Magaz, A.D. Roberts, S. Faraji, T.R.L. Nascimento, E.S. Medeiros, W. Zhang, R.D. Greenhalgh, A. Mautner, X. Li, J.J. Blaker, Porous, Aligned, and Biomimetic Fibers of Regenerated Silk Fibroin Produced by Solution Blow Spinning, Biomacromolecules 19(12) (2018) 4542-4553.
[44] S. Mengistu Lemma, F. Bossard, M. Rinaudo, Preparation of Pure and Stable Chitosan Nanofibers by Electrospinning in the Presence of Poly(ethylene oxide), Int J Mol Sci 17(11) (2016) 1790.

[45] L. Liu, S. Jiang, Y. Sun, S. Agarwal, Giving Direction to Motion and Surface with Ultra-Fast Speed Using Oriented Hydrogel Fibers, Advanced Functional Materials 26(7) (2016) 1021-1027.
[46] J. Schindelin, I. Arganda-Carreras, E. Frise, V. Kaynig, M. Longair, T. Pietzsch, S. Preibisch, C. Rueden, S. Saalfeld, B. Schmid, J.-Y. Tinevez, D.J. White, V. Hartenstein, K. Eliceiri, P. Tomancak, A. Cardona, Fiji: an open-source platform for biological-image analysis, Nature Methods 9(7) (2012) 676-682.
[47] S.-Y. Shin, H.-N. Park, K.-H. Kim, M.-H. Lee, Y.S. Choi, Y.-J. Park, Y.-M. Lee, Y. Ku, I.-C. Rhyu, S.-B. Han, S.-J. Lee, C.-P. Chung, Biological Evaluation of Chitosan Nanofiber Membrane for Guided Bone Regeneration, Journal of Periodontology 76(10) (2005) 1778-1784.
[48] M. Pakravan, M.-C. Heuzey, A. Ajji, A fundamental study of chitosan/PEO electrospinning, Polymer 52(21) (2011) 4813-4824.
[49] N. Bhattarai, D. Edmondson, O. Veiseh, F.A. Matsen, M. Zhang, Electrospun chitosan-based nanofibers and their cellular compatibility, Biomaterials 26(31) (2005) 6176-6184.
[50] S. De Vrieze, P. Westbroek, T. Van Camp, L. Van Langenhove, Electrospinning of chitosan nanofibrous structures: feasibility study, Journal of Materials Science 42(19) (2007) 8029-8034.
[51] B. Duan, C. Dong, X. Yuan, K. Yao, Electrospinning of chitosan solutions in acetic acid with poly(ethylene oxide), Journal of Biomaterials Science, Polymer Edition 15(6) (2004) 797-811.
[52] C. Kriegel, K.M. Kit, D.J. McClements, J. Weiss, Electrospinning of chitosan–poly(ethylene oxide) blend nanofibers in the presence of micellar surfactant solutions, Polymer 50(1) (2009) 189-200.
[53] M. Fernandes Queiroz, K.R.T. Melo, D.A. Sabry, G.L. Sassaki, H.A.O. Rocha, Does the Use of Chitosan Contribute to Oxalate Kidney Stone Formation?, Marine Drugs 13(1) (2015) 141-158.
[54] Y. Wan, H. Wu, A. Yu, D. Wen, Biodegradable Polylactide/Chitosan Blend Membranes, Biomacromolecules 7(4) (2006) 1362-1372.
[55] E. Stodolak-Zych, P. Jeleń, E. Dzierzkowska, M. Krok-Borkowicz, Ł. Zych, M. Boguń, A. Rapacz-Kmita, B. Kolesińska, Modification of chitosan fibers with short peptides as a model of synthetic extracellular matrix, Journal of Molecular Structure 1211 (2020) 128061.
[56] G. Socrates, Infrared and Raman characteristic group frequencies: tables and charts, John Wiley & Sons2004.
[57] M. Rahmati, J.J. Blaker, S.P. Lyngstadaas, J.F. Mano, H.J. Haugen, Designing multigradient biomaterials for skin regeneration, Materials Today Advances 5 (2020) 100051.
[58] Q.P. Pham, U. Sharma, A.G. Mikos, Electrospun Poly(ε-caprolactone) Microfiber and Multilayer Nanofiber/Microfiber Scaffolds: Characterization of Scaffolds and Measurement of Cellular Infiltration, Biomacromolecules 7(10) (2006) 2796-2805.
[59] Q.L. Loh, C. Choong, Three-Dimensional Scaffolds for Tissue Engineering Applications: Role of Porosity and Pore Size, Tissue Engineering Part B: Reviews 19(6) (2013) 485-502.
[60] B.B. Mandal, S.C. Kundu, Cell proliferation and migration in silk fibroin 3D scaffolds, Biomaterials 30(15) (2009) 2956-2965.
[61] R.K.W. Smith, A.E. Goodship, Chapter 2.3 - Tendon and ligament physiology: responses to exercise and training, in: K.W. Hinchcliff, R.J. Geor, A.J. Kaneps (Eds.), Equine Exercise Physiology, W.B. Saunders, Edinburgh, 2008, pp. 106-131.
[62] Z. Li, S. Mei, Y. Dong, F. She, L. Kong, High Efficiency Fabrication of Chitosan Composite Nanofibers with Uniform Morphology via Centrifugal Spinning, Polymers 11(10) (2019) 1550.
[63] B.K. Gu, S.J. Park, M.S. Kim, C.M. Kang, J.-I. Kim, C.-H. Kim, Fabrication of sonicated chitosan nanofiber mat with enlarged porosity for use as hemostatic materials, Carbohydrate Polymers 97(1) (2013) 65-73.
[64] S. Haider, S.-Y. Park, Preparation of the electrospun chitosan nanofibers and their applications to the adsorption of Cu(II) and Pb(II) ions from an aqueous solution, Journal of Membrane Science 328(1) (2009) 90-96.

[65] S.R. Gomes, G. Rodrigues, G.G. Martins, M.A. Roberto, M. Mafra, C.M.R. Henriques, J.C. Silva, In vitro and in vivo evaluation of electrospun nanofibers of PCL, chitosan and gelatin: A comparative study, Materials Science and Engineering: C 46 (2015) 348-358.
[66] C.P. Barnes, S.A. Sell, E.D. Boland, D.G. Simpson, G.L. Bowlin, Nanofiber technology: Designing the next generation of tissue engineering scaffolds, Advanced Drug Delivery Reviews 59(14) (2007) 1413-1433.
[67] L. Martinová, D. Lubasová, Electrospun Chitosan Based Nanofibers, Research Journal of Textile and Apparel 12(2) (2008) 72-79.
[68] I. Yousefi, M. Pakravan, H. Rahimi, A. Bahador, Z. Farshadzadeh, I. Haririan, An investigation of electrospun Henna leaves extract-loaded chitosan based nanofibrous mats for skin tissue engineering, Materials Science and Engineering: C 75 (2017) 433-444.
[69] S.B. Qasim, S. Najeeb, R.M. Delaine-Smith, A. Rawlinson, I. Ur Rehman, Potential of electrospun chitosan fibers as a surface layer in functionally graded GTR membrane for periodontal regeneration, Dental Materials 33(1) (2017) 71-83.
[70] C. Jacquemoud, K. Bruyere-Garnier, M. Coret, Methodology to determine failure characteristics of planar soft tissues using a dynamic tensile test, Journal of Biomechanics 40(2) (2007) 468-475.
[71] A. Ní Annaidh, K. Bruyère, M. Destrade, M.D. Gilchrist, M. Otténio, Characterization of the anisotropic mechanical properties of excised human skin, Journal of the Mechanical Behavior of Biomedical Materials 5(1) (2012) 139-148.
[72] S.G. Guerreiro, C. Brochhausen, R. Negrão, M.A. Barbosa, R.E. Unger, C.J. Kirkpatrick, R. Soares, P.L. Granja, Implanted neonatal human dermal fibroblasts influence the recruitment of endothelial cells in mice, Biomatter 2(1) (2012) 43-52.
[73] Y. Liu, Y. Ji, K. Ghosh, R.A.F. Clark, L. Huang, M.H. Rafailovich, Effects of fiber orientation and diameter on the behavior of human dermal fibroblasts on electrospun PMMA scaffolds, Journal of Biomedical Materials Research Part A 90A(4) (2009) 1092-1106.
[74] F. Yao, W. Chen, H. Wang, H. Liu, K. Yao, P. Sun, H. Lin, A study on cytocompatible poly(chitosan-g-l-lactic acid), Polymer 44(21) (2003) 6435-6441.
[75] J.L. Cuy, B.L. Beckstead, C.D. Brown, A.S. Hoffman, C.M. Giachelli, Adhesive protein interactions with chitosan: Consequences for valve endothelial cell growth on tissue-engineering materials, Journal of Biomedical Materials Research Part A 67A(2) (2003) 538-547.
[76] J. Liu, Q. Fang, X. Yu, Y. Wan, B. Xiao, Chitosan-Based Nanofibrous Membrane Unit with Gradient Compositional and Structural Features for Mimicking Calcified Layer in Osteochondral Matrix, Int J Mol Sci 19(8) (2018) 2330.
[77] H. Ruprai, S. Romanazzo, J. Ireland, K. Kilian, D. Mawad, L. George, R. Wuhrer, J. Houang, D. Ta, S. Myers, A. Lauto, Porous Chitosan Films Support Stem Cells and Facilitate Sutureless Tissue Repair, ACS Applied Materials & Interfaces 11(36) (2019) 32613-32622.
[78] C. Heinemann, S. Heinemann, A. Bernhardt, A. Lode, H. Worch, T. Hanke, In vitro osteoclastogenesis on textile chitosan scaffold, Eur Cell Mater 19 (2010) 96-106.
[79] B.Z. Johnson, A.W. Stevenson, C.M. Prêle, M.W. Fear, F.M. Wood, The Role of IL-6 in Skin Fibrosis and Cutaneous Wound Healing, Biomedicines 8(5) (2020) 101.
[80] M. Baggiolini, P. Loetscher, B. Moser, Interleukin-8 and the chemokine family, International Journal of Immunopharmacology 17(2) (1995) 103-108.
[81] H. Miyagi, S.M. Thomasy, P. Russell, C.J. Murphy, The role of hepatocyte growth factor in corneal wound healing, Experimental Eye Research 166 (2018) 49-55.
[82] F. Sanada, T. Fujikawa, K. Shibata, Y. Taniyama, H. Rakugi, R. Morishita, Therapeutic Angiogenesis Using HGF Plasmid, Ann Vasc Dis 13(2) (2020) 109-115.
[83] P. Italiani, D. Boraschi, From Monocytes to M1/M2 Macrophages: Phenotypical vs. Functional Differentiation, Frontiers in Immunology 5 (2014).

[84] K.H. Hong, J. Ryu, K.H. Han, Monocyte chemoattractant protein-1–induced angiogenesis is mediated by vascular endothelial growth factor-A, Blood 105(4) (2005) 1405-1407.

Graphical abstract

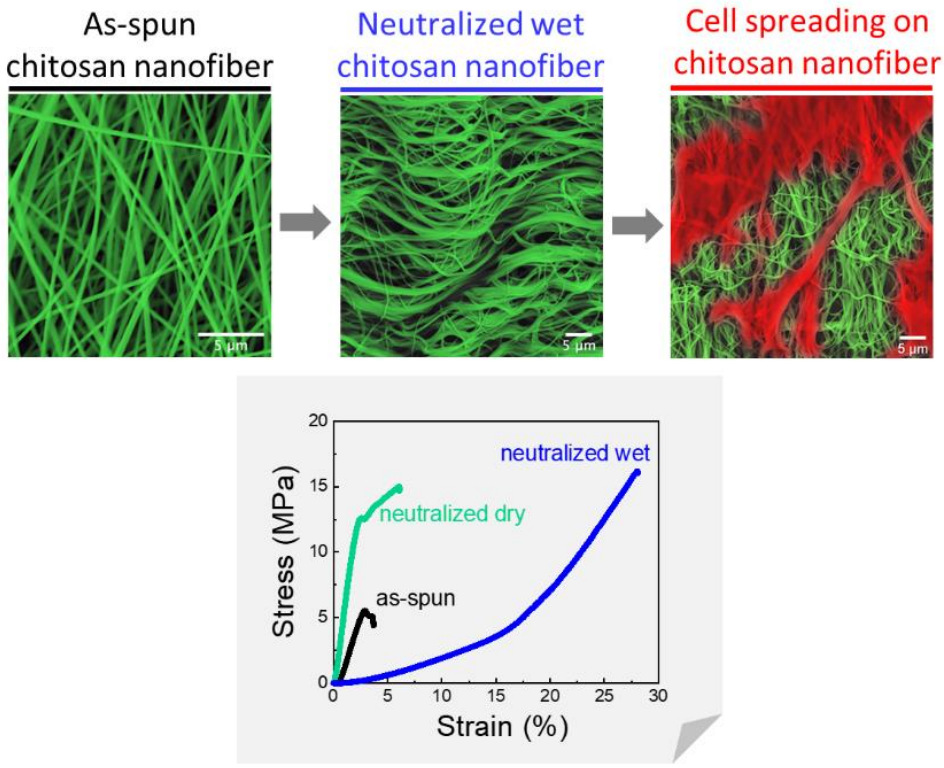

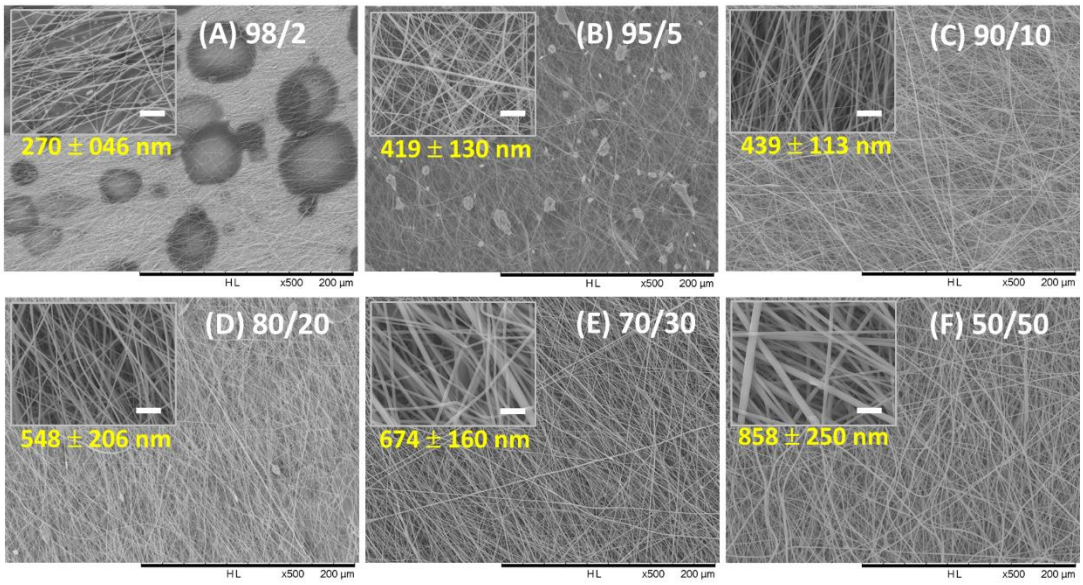

Figure 1. SEM images of chitosan/PEO nanofiber scaffolds at different compositions: (A) 98/2, (B) 95/5, (C) 90/10, (D) 80/20, (E) 70/30, and (F) 50/50. The mean diameter and standard deviation are shown together. Scale bars in inset pictures represent 5 µm.

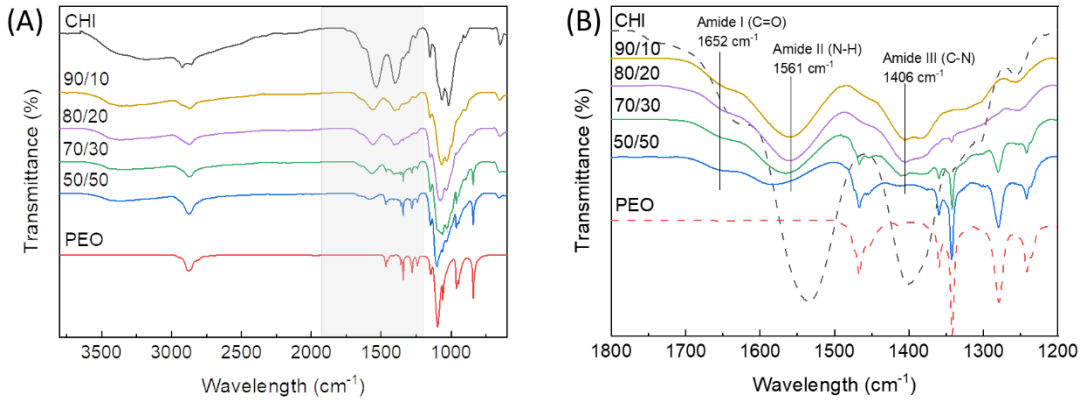

Figure 2. (A) ATR-FTIR results of pure chitosan (CHI), pure PEO, and their chitosan/PEO blend compositions. (B) Enlarged region from the grey box in (A) showing the chitosan amide bands I, II, and III, which in turn confirms the presence of chitosan in all blend nanofiber compositions after SBS.

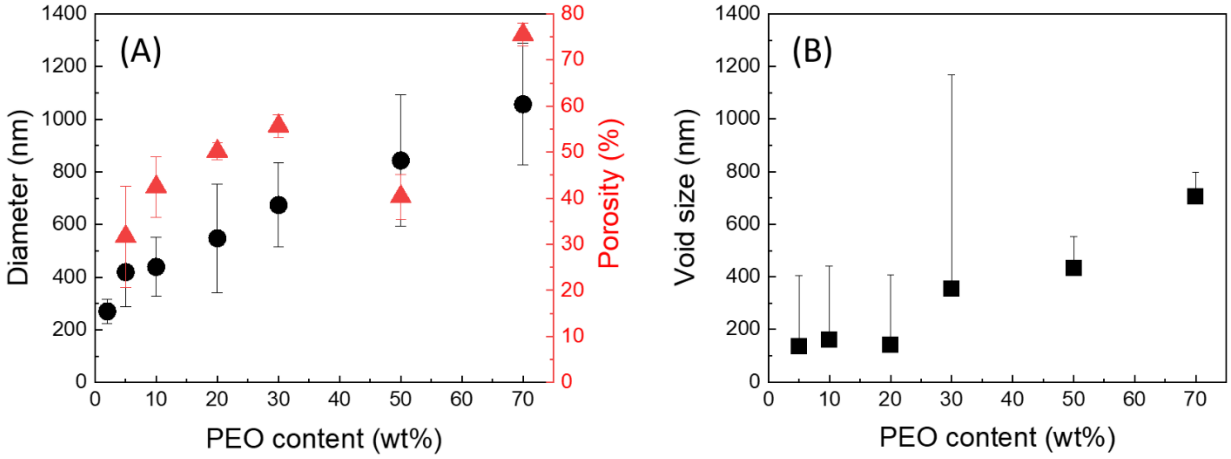

Figure 3. (A) Fiber diameter (●) and porosity (▲) of chitosan nanofiber scaffolds containing different PEO contents and (B) their void size.

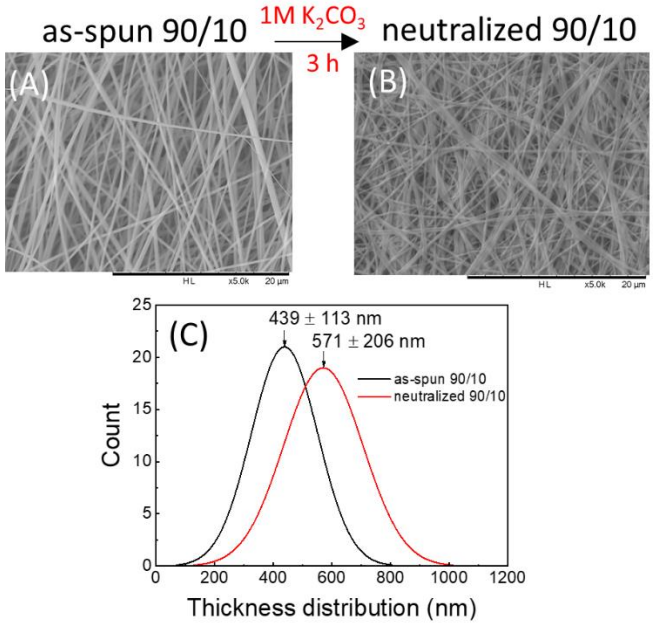

Figure 4. SEM images of the chitosan/PEO (90/10) nanofiber scaffold (A) before and (B) after the potassium carbonate neutralization in 3h. Histogram (C) indicates that the neutralized sample (red curve) gives on average bigger fiber diameter as well as wider thickness distribution than those of as-spun sample (black curve).

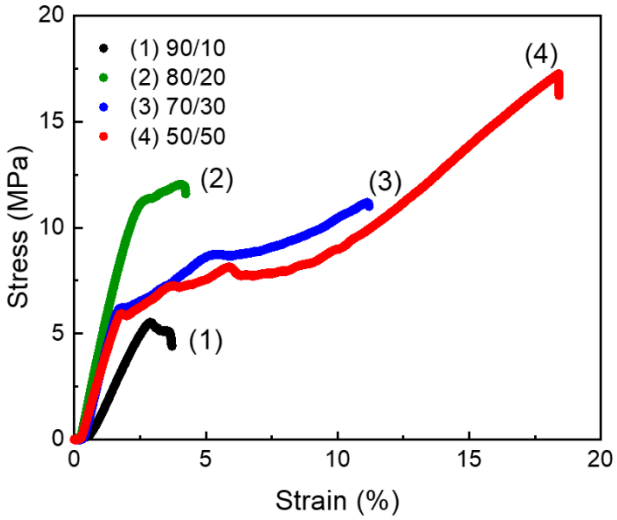

Figure 5. Stress-strain curves of as-spun chitosan nanofiber scaffold containing different PEO content in dry state.

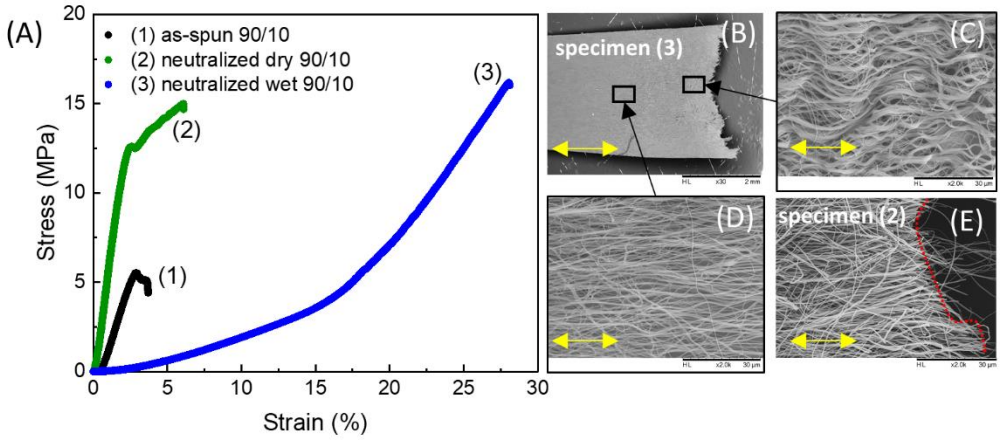

Figure 6. (A) Stress-strain curves of the chitosan/PEO (90/10) nanofiber scaffold in dry and wet states: (1) as-spun 90/10 nanofiber, (2) neutralized dry 90/10 nanofiber, and (3) neutralized wet 90/10 nanofiber. (B) SEM image of the neutralized wet specimen after fracture demonstrate their integral stability and toughness. The magnified images (C, D) represent the black rectangles in (B). (E) SEM image of the neutralized dry specimen after fracture. The red dotted line indicates the fracture site. Horizontal double arrows in SEM images indicate the stretching direction.

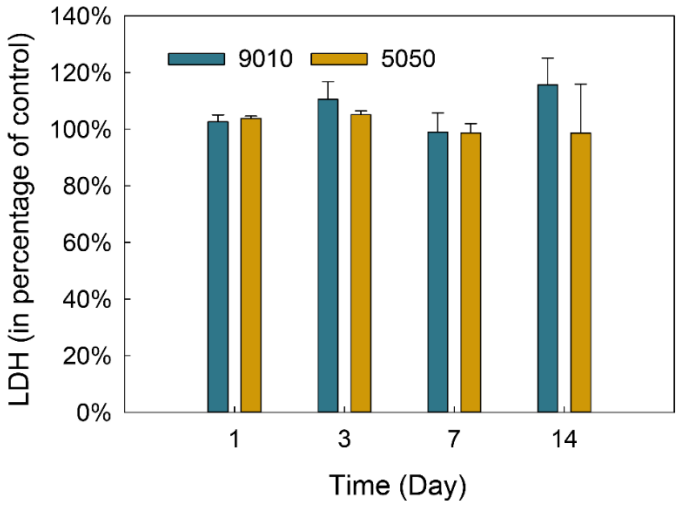

Figure 7. LDH activity in the cell culture media from NHDF cells cultured on neutralized chitosan/PEO 90/10 and 50/50 nanofiber scaffolds for 1, 3, 7, and 14 days. The LDH values are presented in percentage of control group.

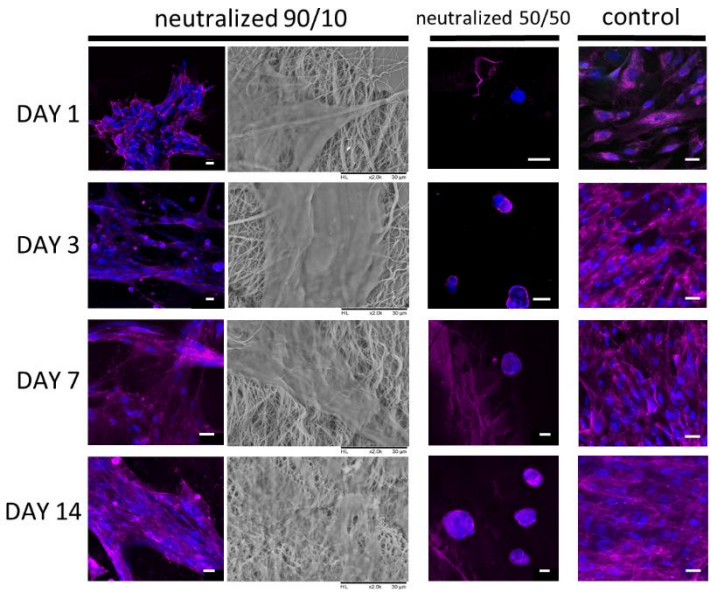

Figure 8. Fluorescence and SEM images of NHDF cells cultured on neutralized chitosan/PEO 90/10 and 50/50 nanofibers for 1, 3, 7, and 14 days. The control samples are immunofluorescence staining of cells seeded on glass coverslips. Cells were stained with WGA-Alexa Fluo 594 (shown in magenta) to label the cell membrane and DRAQ5 (shown in blue) to label the nuclei. Images were acquired sequentially then merged. SEM images demonstrate cells attached onto the scaffolds and spreading. The scale bars in fluorescence images indicate 30 μm.

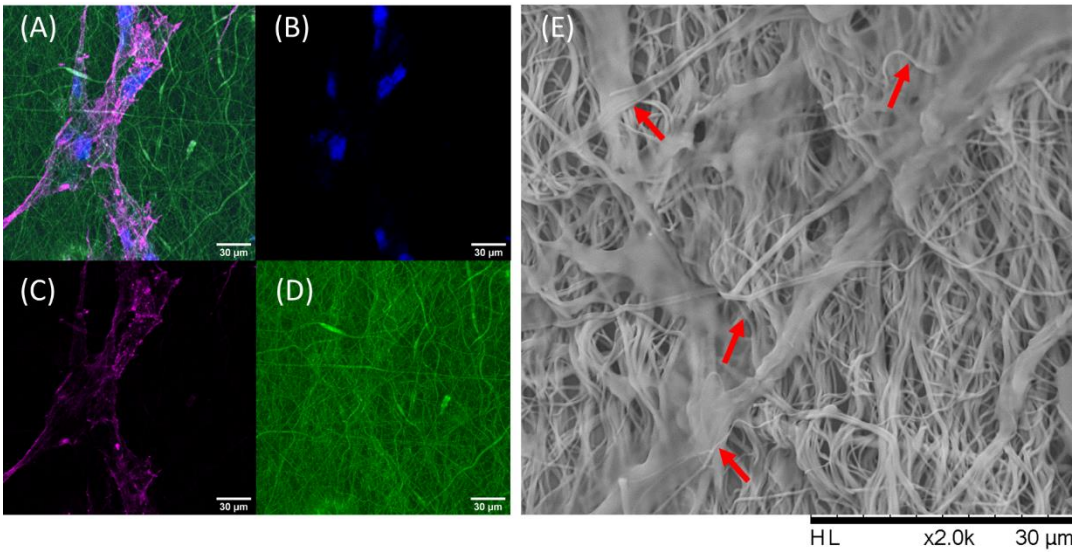

Figure 9. (A) Fluorescence merged image of cells cultured on neutralized chitosan/PEO (90/10) nanofibers where individual channels show (B) cell nucleus (stained with DRAQ5, blue channel), (C) F-actin of cells (stained with phalloidin-Alexa Fluor 568, magenta channel), and (D) nanofibers (green channel). (E) Representative SEM image. Red arrows in (E) indicate fibers seen on the surface of cell spreading regions.

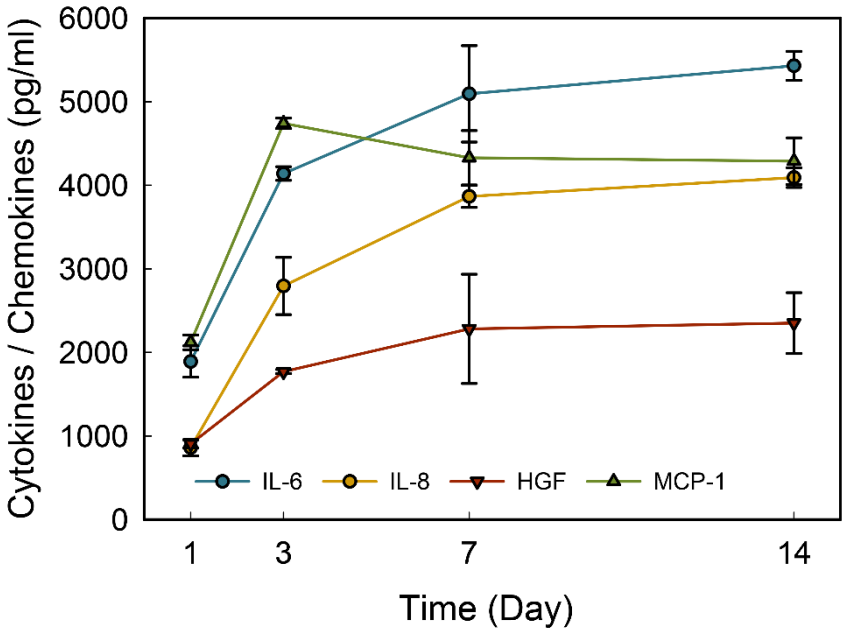

Figure 10. Secretion profiles of IL-6, IL-8, HGF, and MCP-1 proteins in the cell culture media from NHDF cells cultured on the neutralized chitosan/PEO 90/10 scaffold for 1, 3, 7, and 14 days.

Supporting Information

Solution blow spinning of highly deacetylated chitosan nanofiber scaffolds for dermal wound healing

Nguyen D. Tien[1], Tianxiang Geng[1], Catherine A. Heyward[1], Janne E. Reseland[1], S. Petter Lyngstadaas[1], Jonny J. Blaker[1,2*], Håvard J. Haugen[1*]

[1]Department of Biomaterials, Institute of Clinical Dentistry, University of Oslo, 0317 Oslo, Norway
[2]Department of Materials and Henry Royce Institute, The University of Manchester, Manchester, M13 9PL, United Kingdom

*Correspondence: h.j.haugen@odont.uio.no; jonny.blaker@manchester.ac.uk

Thermogravimetry analysis (TGA)

The thermal properties of the nanofibers were analyzed by TGA using a Hitachi STA300 instrument (Hitachi, Japan) and used to evidence the presence of chitosan and PEO in the obtained fiber mats. Scans were made from 25 °C to 800 °C with a heating rate of 10 °C/min, under an N_2 flux, to prevent thermo-oxidative processes. The results are discussed and shown in Figure S1. The weight loss and their derivative profiles (DTG) were obtained to identify the actual weight composition (Table S1) and the main degradation peaks of the nanofibers.

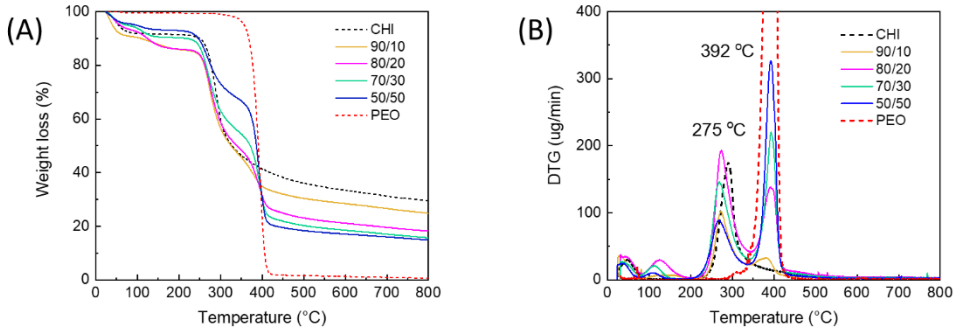

Figure S1. Comparison of (A) TGA curves and (B) their derivative profiles of pure chitosan (CHI), pure PEO, and their chitosan/PEO blend nanofibers.

The thermal stability of the chitosan/PEO nanofiber scaffolds at different compositions was studied by TGA. The profiles of neat chitosan and PEO are shown together for comparison. All thermogravimetric curves are shown in Figure S1A, and their first derivative curves are shown in Figure S1B.

One stage of mass loss is seen for pure PEO with degradable temperature of 392 °C, while two stages are observed for pure chitosan. The first stage (below 150 °C) is associated with the loss of residual acetic acid while the second stage is associated with the major weight loss at maximum degradation temperate of 290 °C, indicating the decomposition of chitosan structures. It can be concluded that pure chitosan demonstrated lower thermal stability than pure PEO.

On the other hand, all blend nanofibers showed three stages of mass loss which attributed to the loss of residual solvent (below 150 °C), the chitosan structures (around 275 °C, slightly slower than that of pure chitosan due to chitosan-PEO interaction), and the PEO backbone (around 392 °C). The average weight loss of 10% for all blends is attributed to the residual acetic acid and moisture drying phase within the nanofiber network. The higher content of chitosan, the larger mass loss due to the higher amount of acetic acid. Two major mass losses related to chitosan and PEO degradation are clearly seen with the relative weight loss is depended on the blend compositions. Interestingly, while the constant weight percentage of PEO is almost zero at 800

°C, around 30% residue of pure chitosan and 15–25% residue of blends remain. Therefore, TGA results are used to quantify further the apparent weight composition of blend nanofibers after the spinning process, which is reported in Table S1. The calculation is achieved by measuring the related area under the peaks of chitosan and PEO in the first derivative of the TGA curves (Figure S1B) without considering the residual solvent and ash level in the mats. Such increase of PEO content in the nanofiber mats compared to those in the prepared solution suggests a better spinnability of PEO than that of chitosan. These results agree with the literature values [1].

Table S1. Comparison of the composition of chitosan/PEO in spinning solution and in nanofiber mat calculated from derivative of TGA curves by peak area analyses

Sample	Composition in spinning solution	Residue (wt%)	Apparent composition in nanofibers (peak area)
Chitosan	-	29.5	-
PEO	-	0.6	-
chitosan/PEO	90/10	24.7	83.9/16.1
	80/20	18.2	64.5/35.5
	70/30	15.7	51.2/48.8
	50/50	14.8	33.0/67.0

^{1}H-Nuclear Magnetic Resonance (^{1}H-NMR)

^{1}H-NMR of chitosan nanofibers was recorded on a Bruker AVIII-HD400 spectrometer at 400 MHz (Bruker, Wissembourg, France). Deuterium chloride (DCl) 35 wt% in deuterium oxide (D_2O) solution (Sigma-Aldrich) was used as solvent. Nanofiber samples of 3 to 5 mg were dissolved in 1 mL of DCl 35 wt% in D_2O and placed inside a 5 mm diameter NMR test tube (Standard series, NORELL Inc., Morganton, NC, USA). ^{1}H-NMR was performed with 16 scans at 25 °C.

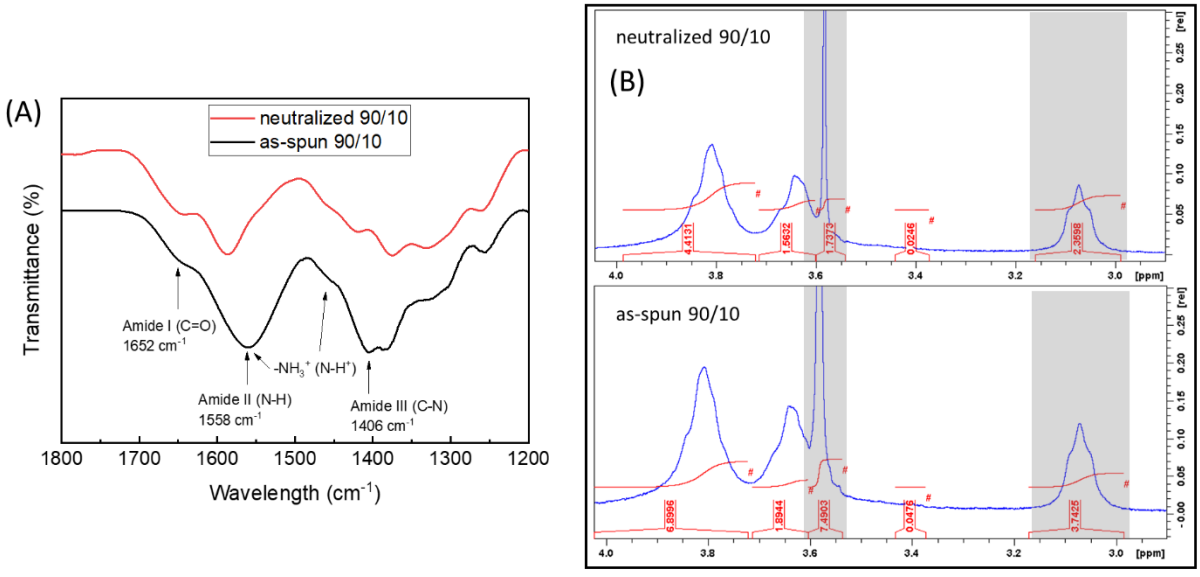

Figure S2. (A) ATR-FTIR spectra and (B) ^{1}H-NMR of the chitosan nanofiber scaffold before and after the potassium carbonate neutralization in 3 h. In FTIR, the presence of ion $-NH_3^+$ on the nanofibers is noticed, and its intensity decreases after neutralization. In ^{1}H-NMR, the PEO extraction was confirmed by observing the ratio of proton integral of the $-CH_2-$ group in PEO (chemical shift ~ 3.58 ppm) and in chitosan (chemical shift ~ 3.08 ppm) for the neutralized 90/10 sample is 7.49/3.74 suppressed drastically to 1.74/2.36 for the as-spun 90/10 sample.

Reference

1. P. Kianfar, A. Vitale, S. Dalle Vacche, R. Bongiovanni, Photo-crosslinking of chitosan/poly(ethylene oxide) electrospun nanofibers, Carbohydrate Polymers 217 (2019) 144-151.